Statistical analysis of the pitting corrosion induced by potentiostatic pulse tests of wrought and SLM 316L stainless steels

Arthur Racot, Isabelle Aubert, Marie Touzet, Stéphanie Thiebaut, Michel Demesy

Version of Record: https://www.sciencedirect.com/science/article/pii/S0010938X21008040
Manuscript_de848cb828b040bd9a1ebf899584ca10

Statistical analysis of the pitting corrosion induced by potentiostatic pulse tests of wrought and SLM 316L stainless steels

Arthur Racot[a], Isabelle Aubert[a,*], Marie Touzet[b], Stephanie Thiebaut[c], Michel Demesy[c]

[a] *University of Bordeaux, CNRS, Arts et Metiers Institute of Technology, Bordeaux INP, INRAE, I2M Bordeaux, F-33400 Talence, France*
[b] *Bordeaux INP, University of Bordeaux, CNRS, Arts et Metiers Institute of Technology, INRAE, I2M Bordeaux, F-33400 Talence, France*
[c] *CEA, DAM, Valduc, 21120 Is-sur-Tille, France*

Abstract

An original approach coupling potentiostatic pulse tests and statistical analysis of the pitting features was carried out to compare the sensitivity to pitting corrosion of wrought and SLM 316L SS (stainless steels). The measurement and analysis of current densities during potentiostatic pulse tests has led to a better understanding of the pitting corrosion behavior of wrought and SLM 316L SS in 4 mol.l−1 NaCl solution at 50 °C. The association of global measurements and local observations showed that the two stainless steels exhibit different pitting mechanisms. Moreover, a slightly different susceptibility to pitting corrosion is found between the direction of manufacture and the normal direction for the 316L SLM with these tests. The role of the microstructure and the passive film in the pitting corrosion behavior is

*corresponding author. University of Bordeaux, CNRS, Arts et Metiers Institute of Technology, Bordeaux INP, INRAE, I2M Bordeaux, F-33400 Talence, France, +335 40 00 22 97 ; fax +335 40 00 69 64
Email address: isabelle.aubert@u-bordeaux.fr (Isabelle Aubert)

discussed.

Keywords:

316L stainless steel, Selective Laser Melting (SLM), Pitting corrosion, Potentiostatic pulse test, Microstructure, Passive film, Statistical analysis

---

1. Introduction

Additive Layer Manufacturing (ALM) processes are booming in the recent years. A new range of possibilities are provided for the design of stainless steel net shape parts with complex geometries and multi-scale structural patterns like lattice structures [1, 2, 3].

Selective Laser Melting process (SLM) consists in stacking metal powder layers fused by a laser [4, 5, 6, 7]. This additive manufacturing technique allows the production of dense parts with great mechanical properties when the parameters are optimal. Otherwise, defects like porosities, unmelted powder residues and oxides can be created. Therefore, it is important to optimize the manufacturing parameters to avoid creating too many large defects [8]. Austenitic stainless steels produced by additive manufacturing are very interesting because they are widely used in many industrial fields thanks to their high ductility and their excellent corrosion resistance [9, 10]. AISI 316L stainless steel microstructure obtained by SLM depends on the powder characteristics and the process. Nevertheless, an anisotropy of size and morphology of grains is always noticed [11, 12]. Indeed, grains are columnar in the build direction while no particular grain shape appears in the normal direction. In addition, when chemical or electrochemical attack is carried out to reveal the grains, the microstructure exhibits melt pool which is typical

of materials manufactured by these technologies [13, 14]. Furthermore, SEM observations reveal a submicronic cellular-dendritic substructure inside the grains [13, 15, 16, 17, 14, 12, 18, 19].

Corrosion resistance of AISI 316L is due to the passive film formation. This oxide layer, mainly composed of Cr_2O_3, has a low permeability which limits the transfer, towards the interface beetween steel and the inner oxide, of aggressive agents from the surrounding environment [20].

Only a few recent studies focused on the corrosion sensitivity of the AISI SLM 316L stainless steel in NaCl solutions at various concentrations and in simulated body fluid (SBF) [21, 14, 22, 23, 24, 25, 26]. Among the defects present in a SLM part, namely porosities, unmelted powder residues and oxides, Man et al [27] showed, using analysis of SEM surface before and after polarization tests, that only powder residue type defects were pitting initiation sites. Other studies showed, using potentiodynamic tests, that a no-defect 316L steel obtained by SLM was more resistant to corrosion than wrought 316L steel. Sander et al. [21] highlighted, using cyclic polarization curves, that regardless of manufacturing parameters, the pitting corrosion resistance of SLM 316L steel was much higher than that of wrought 316L steel. While anisotropy of microstructure and mechanical properties were examined, only few studies investigated the effect of the manufacturing direction on the corrosion resistance (build direction (BD) and normal direction (ND)) of SLM 316L, and in this case, no difference in corrosion susceptibility was observed [28].

However, it is important to better understand pit initiation mechanisms when the SLM 316L presents few process-related defects. Therefore, the ef-

fect of the manufacturing process on the material microstructure and the susceptibility to pitting corrosion are considered in the current study. To achieve these goals, an analysis of the microstructure is first presented. Then, the study of the corrosion pitting sensitivity is carried out using global electrochemical techniques and potentiostatic pulse tests (PPT) [29, 30, 31, 32, 33]. This technique has been used to identify the precursor sites of pitting corrosion [34], to investigate the effect of the manufacturing process and the impact of surface treatments on pitting susceptibility of stainless steels [29, 35]. In our case, PPT are particulary appropriate because they induce the initiation of a high density of small pits on the surface of the sample [31]. In addition, PPT allow us to cause the first degradation stages of the passive film in contrast to electrochemical impedance spectroscopy (EIS) [36, 30]. A statistical study of the damage generated by the potentiostatic pulse tests is performed to evaluate the effect of additive manufacturing and its anisotropy on the pitting corrosion sensitivity for the AISI 316L. In addition, an analysis of the current density response recorded during the pulse tests is carried out in order to provide informations on the initiation, propagation and mechanisms of pitting.

2. Material and methods

2.1. Specimens and surface preparation

Experiments were performed on wrought and additive manufactured austenitic AISI 316L stainless steel (grade X2CrNiMo17.12.2). Wrought 316L was supplied as a 2 mm thick cold-rolled annealed sheet by Sapim Inox. Its chemical composition (wt%) was measured by optical emission spectrometry for ele-

ments Cr, Mn, Mo, Ni, P, Si and by combustion infrared absorption method for elements S, C. The composition expressed in weight percent is given in Table 1. The SLM 316L sample was produced by GMP Additiv using an EOS M290 with an Yb-fiber laser (1070 nm) having a fixed laser diameter of 100 μm. Parameters provided by EOS were optimised, in particular the thickness of the layer was set at 40 μm. AISI 316L stainless steel powder with a spherical particule size distribution from 10 to 45 μm was supplied by Oerlikon mecto GmbH. Chemical composition (wt%) of SLM 316L is given in Table 1. Specimens were cold coated in epoxy resin EpoFix supplied by Struers then polished with silicon carbide (SiC) papers up to 2500 grit and polished with diamond suspensions (3 and 1 μm). An ultrasonic bath was used between each step to thoroughly clean the specimens. For electron-backscattered diffraction (EBSD) observations, a final polishing was carried out with colloidal silica suspension of 0.1 μm.

2.2. Surface characterization and XRD measurements

To reveal the microstructural features, the polished 316L specimens were etched for 10 min in 100 ml HCL + 100 ml H_2O + 10 ml HNO_3. The microstructural analysis of the SLM and wrought specimens was carried out using two optical microscopes (Olympus PMG 3 and Keyence VHX-7000) and a scanning electron microscope (SEM)(Zeiss EVO HD15). Electron-backscattered diffraction (EBSD) was performed using an EDAX's TEAM^{TM} EBSD Analysis System with OIM Analysis^{TM} software. The EBSD observations were conducted at 15 kV, 3 nA, at a working distance of 18 mm with a step of 2 μm and cleaned by dilatation by assigning the areas of less than 3 pixels to the nearest grain. Observations were carried out in the build and

in the normal directions of SLM 316L and on wrought 316L (Fig. 4). Transmission electron microscope observations of wrought 316L were performed with a Philips CM20FEG operating at 200kV with a Schottky field emission gun. Energy Dispersive Spectroscopy (EDS) maps were obtained with a SDD Bruker detector with an energy resolution of 127eV. A 2 nm diameter probe was used and a resolution of one measure every 10 nm was chosen. To determine residual stresses in wrought and SLM 316L, the samples were vertically cut in the middle of the specimen and measurements were performed in the center of the material. Residual stresses were measured using a Bruker D8 Discover Xray diffractometer equipped with a 2D detector. To investigate the SLM and wrought 316L the austenite (311) diffraction peak was chosen with the 2θ range between 107° - 115,5° at a step size of 0.1°. The sample was rotated about the Φ axes and tilted about Ψ axes to evaluate all the components of the stress tensor. The magnitude of residual stress was determined using the fundamental method at 8 Φ angles (0°, 45°, 90°, 135°, 180°, 225°, 270°, 315°) and at 4 Ψ angles (0°, 20°, 40°, 60°). To calculate the residual stress, the constant used are Young's modulus of 200 GPa, Poisson ratio of 0.28, s1 = -2.0.10-6 MPa^{-1} and 1/2s2 =7.0.10-6 MPa^{-1}. The samples were vertically cut in the middle of the specimen to determine residual stresses in the center of the material.

2.3. Cyclic potentiodynamic polarization and Potentiostatic pulse testing

Cyclic potentiodynamic polarization and Potentiostatic pulse tests were carried out using an electrochemical workstation (Ametek VersaSTAT 3F type). A steel wire was fixed at the bottom of each sample to ensure the electrical connection. To prevent crevice corrosion during electrochemical

tests, the epoxy/sample interface was insulated using varnish. A conventional three electrode method was used to carry out the electrochemical measurements. Electrochemical potential was measured vs. Ag/AgCl (saturated solution) and the counter electrode was made of a platinum grid. Preliminary tests were conducted in NaCl solution by varying the concentration from 0.6 mol.l^{-1} to 4 mol.l^{-1} and the temperature range from 25 °C to 50 °C to select the right experimental conditions which ensure to remain in the pitting conditions and not in the transpassive domain for the cyclic polarization tests and PPT [31]. Due to their high corrosion resistance, the studied materials were finally tested in 4 mol.l^{-1} NaCl solution at 50 °C. Prior to polarization and PPT, specimens were immersed in the electrolyte during 30 min at open circuit potential (E_{ocp}).

The cyclic potentiodynamic polarisation tests were performed using a scan rate of 1 mV/s, from a potential of -0.1V/ E_{ocp} to a current density value fixed at 0.1 mA.cm^{-2}. Then, the scanning direction was reversed up to the initial potential value. The test was repeated 3 times for each specimen to ensure reproducibility and consistency of the collected data.

Two different PPT were conducted. First, single pulse tests were carried out, which consisted in applying, during 1, 2 or 4 seconds, a potential jump of 300mV from the pitting potential (E_{pit}) followed by a return to the repassivation potential (E_{rep}) during 2s (Fig. 1 (a)). Then, cyclic PPT were performed by applying 10, 20 and 30 times the following cycle : a potential jump of 300mV from the pitting potential (E_{pit}) was applied during 2 seconds and followed by a return to the repassivation potential (E_{rep}) during 2s (Fig. 1 (b))

After these tests, specimen surface was systematically observed by optical microscopy and scanning electron microscopy to make a statistical analysis of the pitting corrosion.

Additional PPT were conducted to identify the initiation sites in the microstructure of wrought 316L. As in the previous PPT, 30 cycles were applied by varying the potential between E_{pit} + 300 mV and E_{rep}. The difference between both tests was the duration of each part of the cycles: it was reduced to 0.75 s to initiate smaller pits. After this test, specimens were etched for 10 min in 100 ml HCL + 100 ml H_2O + 10 ml HNO_3 and the surface was observed by optical microscopy and scanning electron microscopy.

2.4. Statistical analysis

After polarization and PPT, the specimen surface was observed by optical microscopy and scanning electron microscopy to make a statistical analysis of the pitting corrosion. This analysis was carried out using ImageJ to count the number of pits and measure their size on a sufficient number of images to carry out a statistical approach (10 images of size 2133 x 1600 μm^2). The tests were repeated on 3 samples to verify the reproducibility of the test. The presented results gathered data obtained from 30 images corresponding to cumulated area of 34 mm^2 for each sample. The normalized pit density was plotted in a bar graph as a function of pit size distribution in diameter. All relative density histograms were represented using the same scale. Experimental distributions were discretized using the same interval of 1.25 μm. The minimum size for the detection of pits is 5 μm. Depending on the shape of the pit size distribution, a normal or log-normal distribution law defined by the following probability densities (eq. 1 and eq. 2) was associated:

$$normal : f(x) = \frac{1}{\sigma\sqrt{2\pi}} e^{-\frac{1}{2}\left(\frac{x-\mu}{\sigma}\right)^2} \quad (1)$$

$$log - normal : f(x) = \frac{1}{\sigma_{ln(x)} x\sqrt{2\pi}} e^{-\frac{1}{2}\left(\frac{ln(x)-\mu_{ln(x)}}{\sigma_{ln(x)}}\right)^2} \quad (2)$$

where μ and σ are respectively the mean and standard deviation of the variable x and $\mu_{ln(x)}$ and $\sigma_{ln(x)}$ are respectively the mean and standard deviation of the variable ln(x).

For each cyclic PPT, the mean diameter and its standard deviation were well approximated by the corresponding normal or log-normal law. This is crucial for calculating unbiased averages and 95% confidence intervals.

3. Results

3.1. Microstructure

Micrographs of wrought 316L steel reveal a microstructure composed of equiaxed grains (Fig. 2a and Fig. 3a). The optical micrographs of SLM 316L stainless steel (Fig. 2b and 2c) display a microstructure characteristic of metals obtained by selective laser melting [13, 14]. Indeed, melt pools linked to the laser passes are seen along the build directions (Fig. 2b) and the laser passes are observed along the normal direction (Fig. 2c).

EBSD maps of the SLM 316L (Fig. 3), show the presence of columnar grains oriented in the build direction (Fig. 3b) and grains without particular shape in the normal direction (Fig. 3c). According to the literature, submicronic cellular-dendritic substructures inside the grains are revealed by

SEM micrographs (Fig. 5) [15, 16, 17, 12, 18, 19]. The appearance of such a substructure could be linked both to multiple rapid and successive melts and coolings [13] and to a difference in chemical composition due to the low kinetics of homogenisation of bigger atoms. Indeed, studies showed through transmission electron microscope observations (TEM) that there is a high concentration of dislocations and Mo enrichment within cellular-dendritic structure [12, 25].

3.2. Cyclic potentiodynamic polarization

The cyclic polarization curves of wrought 316L and SLM 316L in build direction (BD) and normal direction (ND) immersed in 4 mol.l $^{-1}$ NaCl at 50 ° C are shown in Fig. 6. Regardless of the tested sample, a characteristic passivity plateau is observed in the anodic part of the curve. No instability related to the development of metastable pitting is observed on the cyclic polarization curves of the stainless steel. For each sample, the corrosion potential (E_{corr}), the pitting potential (E_{pit}), the repassivation potential (E_{rep}) and the passivity plateau ΔE (E_{pit}-E_{corr}) are extracted from the polarisation curves and reported in Table. 2. The corrosion and repassivation potentials of the 316L SS does not depend neither on the manufacturing process nor on the building direction for the SLM specimens .

The passivity plateau is followed by a sharp increase in current density from the pitting potential (E_{pit}). This is due to the rupture of the passive film and to the development of pits on the 316L SS surface. The value of E_{pit} is significantly higher for the steel obtained by SLM. Indeed, E_{pit} for wrought steel is 108 ± 16 $mV_{AgCl/Ag}$ while for additive manufactured steel it is approximately 600 $mV_{AgCl/Ag}$. These results are consistent with those of

the literature showing that the SLM 316L is less sensitive to pitting corrosion than wrought 316L [25, 21, 22].

The sizes of the passivity plateau ($\Delta E = E_{pit}$ - E_{corr}) does not bring out significant differences between BD and ND SLM 316L. The calculation of the 95% confidence interval of the pitting potential does not highlight any effect of the SLM 316L faces orientation on the pitting corrosion sensitivity.

3.3. Potentiostatic pulse tests

3.3.1. Single potentiostatic pulse tests

Cyclic polarization tests allow the selection of the operating conditions for the PPT. Indeed, it is possible to choose a potential that ensures the steel depassivation (E_{pit} + 300) $mV_{AgCl/Ag}$ and also the potential that allows the repassivation (E_{rep}). A potential of 900 $mV_{AgCl/Ag}$ is selected for SLM 316L because its pitting potential is about 600 $mV_{AgCl/Ag}$. A potential of 400 $mV_{AgCl/Ag}$ is selected for wrought 316L which has a pitting potential of about 100 $mV_{AgCl/Ag}$.

During the test, the potential is imposed and the current response is measured. This current density can provide informations on the susceptibility of the material to pitting corrosion and the damage mechanisms.

Fig. 7 shows the current density response for single PPT of different durations for wrought 316L and SLM 316L in the build and normal directions. It is worth noting that the current density responses of wrought and SLM 316L are completely different. Indeed, the scale of the current density of the wrought sample is 5 times higher than that of SLM samples. Moreover, for the wrought 316L, an incubation time is observed before a gradual increase of the current density with the potential pulse time (Fig. 7a, 7d and 7g).

For SLM 316L in both BD and ND directions, the current density increases sharply at the beginning of the potential disturbance and then decreases during the potential pulse time of 1s (Fig. 7b and 7c). When the perturbation is maintained for 2 and 4 s, the current density for ND SLM 316L rises again (Fig. 7f and 7i) while it continues to decrease for the BD SLM 316L (Fig. 7e and 7h). This difference between current response to a potential disturbance for wrought 316L and the SLM 316L can be completed with SEM observations. Fig. 8 clearly shows that the increase of the pulse duration leads to an increase of the pit size for wrought 316L (Fig. 8a, 8d and 8g), whereas for SLM 316L in both directions of manufacturing, the pit sizes are independant of the pulse duration (Fig. 8b, 8e and 8h and 8c, 8f and 8i). The mean pit density and pit diameter are determined from the statistical analysis based on the surface observation after the pulse tests.

Fig. 9a shows the density of electric charge (calculated from the colored area under the current density response curve in Fig. 7), the pit density (Fig. 9b) and the average pit diameter (Fig. 9c) obtained for the 1, 2 and 4 s tests. It is noticed that the density of electric charge (Fig. 9a) increases for the wrought 316L, whereas, only a very small increase is seen for ND SLM 316L and no increase is observed for the BD SLM 316L. For a 1s pulse duration, every sample presents the same very low level of density of electric charge but after a potential pulse of 2s and 4s, the density of electric charge of wrought 316L is 10 to 100 times higher than that of SLM 316L.

It can be seen that the pit density of wrought 316L is four times higher than that of SLM 316L (Fig. 9b). Moreover, regardless of the sample, this density is independant of the pulse duration. This means that when the

potential jump of E_{pit} + 300 mV is maintained, no new pits are created other than those initially produced by this disturbance. Thus, the increase of density of electric charge of wrought 316L is essentially due to the growth of pits, previously seen in Fig. 8a, 8d and 8g. A growth of pit mean diameter is seen for the wrought 316L, while for SLM 316L it is not observed (Fig. 9c).

These single pulse tests show that wrought and SLM 316L do not have the same damage mechanisms. The SLM 316L could passivate again while maintaining a potential beyond its pitting potential. In addition, a slight difference of current density response can be observed between BD SLM 316L and ND SLM 316L (Fig. 7e, 7f, 7h and 7g).

3.3.2. Multiple potentiostatic pulse tests

Fig. 10 shows the current density as a function of the number of potential pulses for each material. The shape of the current response seen in Fig. 7 is found again for cyclic pulses for each material.

An increase of the maximum current density peak is observed for wrought 316L during the first four pulses, (Fig. 10a). It is followed by a decrease of this peak which becomes lower and lower corresponding to an electric charge density which becomes negligible.

A different behavior is observed for the SLM 316L. A slight increase of the maximum current density peak is seen for each pulse during the entire test (Fig. 10b and 10c). The maximum peak value increases from 0.01 $A.cm^{-2}$ to 0.025 $A.cm^{-2}$ for BD SLM 316L (Fig. 10b) and from 0.015 $A.cm^{-2}$ to 0.04 $A.cm^{-2}$ for ND SLM 316L (Fig. 10c). In addition, it can be observed a pro-

gressive occurence of a second peak after relaxation for ND SLM 316L. The latter increases between ten and twenty pulses and then remains constants until the end of the test (Fig. 10c). An example of wrought and SLM 316L surfaces after twenty pulses is shown in Fig. 11 where the pits are visible. A statistical analysis of the sample surface is proposed to quantify the damage reflected during the multiple pulse tests.

The pitting density as a function of the number of pulses is presented in Fig. 12. It increases for the different materials and orientations with the number of pulse repetitions. An increase of small pits is seen as a function of pulse repetition for wrought 316L. Indeed, the formation of numerous pits around 30 and 40 μm is observed for 10 pulses while for 20 and 30 pulses, great number of pits less than 30 μm are initiated (Fig. 12a). Regarding for the SLM 316L, a difference is visible between the build and normal direction. For both materials, the range of pit diameter is the same and is independent of the number of pulse repetitions but the number of pits increases more significantly for ND SLM 316L than for BD SLM 316L, which means that more defects are created on the surface of SLM 316L steel in the normal orientation. It is worth noting that wrought 316L steel has a different pitting size distribution than additive manufactured steel.

Pit distribution laws are shown in Fig. 13 for all multiple pulse tests. Regarding the wrought 316L, a shift of the average size of the pits is noticed. The distribution law changes from a normal distribution law for 10 pulses centered around 34 μm (Fig. 13a) to a log-normal distribution law for 20 and 30 pulses respectively centered around 29 μm and 28 μm (Fig. 13d and 13g). No pit average shift is observed for BD and ND 316L SLM. Indeed,

the normal laws are centered around the same value for 10, 20 and 30 pulses for the 316L SLM in both manufacturing directions (Fig 13b, 13c, 13e, 13f, 13h and 13i).

With the help of these distribution laws, the means of the pit diameter and the 95% confidence intervals are determined and represented in Fig. 14 (c).

Fig. 14 (a) shows the density of electric charge (area under the current density response curve Fig. 10), the pitting density (Fig. 14 (b) and the average pitting diameter (Fig. 14 (c)) obtained as a function of the pulse number. These graphs confirm that the wrought 316L is more sensitive to pitting than the SLM 316L, but they also allow us to highlight the differences of pitting susceptibility of BD and ND SLM 316L. Indeed, a greater increase in electrical charge density and pitting density is observed for the ND SLM 316L than for the BD SLM 316L (Fig. 14 (a) and (b)), whereas, the average pit size is the same for both directions. These tests allow us to conclude that ND SLM 316L is more susceptible to pitting corrosion than BD SLM 316L (Fig. 14 (c)). Surface analyzes (Fig. 12 and 14) and current density response (Fig. 10) show that the second depassivation observed for ND SLM 316L (Fig. 10) leads to the creation of new pits without increasing the size of the existing ones since the average pit size remains constant for 10, 20 and 30 pulses.

A small increase in charge density of about 10% is observed for wrought 316L between 10 and 30 pulses (Fig. 14 (a)) while a larger increase in pitting density (Fig. 14 (b)) and a decrease in the average pit size (Fig. 14 (c)) are jointly observed. The first pulses with high current densities (Fig. 10) will

create large pits. Then smaller pits will be created later when the current density becomes lower (Fig. 10).

4. Discussion

4.1. Electric charge density versus pit nucleation

The aim of the model proposed in this section is to assess that the current density measurements during the PPT are consistent with the pitting initiation and growth observed in the sample surface.

A comparison between the experimental electric charge density measured during PPT ($C_{corr-exp}$) and the theoretical electric charge density produced by the nucleation of pits (C_{corr}) is proposed. Following calculations have been performed in the case of the 2 s single PPT. The corroded volume of one pit created during the 2s single PPT (Vol_{1pit}) is calculated from the geometry of the mean pit (Eq. 3) by assuming, in first approximation, a spherical cap shape (Fig. 15). The current density associated to the corrosion of one spherical cap $J_{corr1pit}$ is obtained using the Faraday's Law (Eq. 4). Then, the total current density (J_{corr}) (Eq. 5) expected for the analyzed sample surface (S_{tot}) is obtained by taking into account the pit density ($Pit_{density}$). Finally, the density of electric charge (C_{corr}) induced by the 2s single PPT is given by (Eq. 6). The pit density, the mean pit diameter, the pit depth as well as the density of electric charge measured during PPT are obtained experimentally.

$$Vol_{1pit} = \frac{\pi * h^2(3r - h)}{3} \tag{3}$$

$$j_{corr_{1pit}} = \frac{Vol_{1pit}}{\Delta t} * \frac{\rho_{Fe}}{M_{Fe}} * \frac{2F}{S_{1pit}} \tag{4}$$

$$j_{corr} = j_{corr_{1pit}} * Pit_{density} * S_{tot} \tag{5}$$

$$C_{corr} = j_{corr} * \Delta t \tag{6}$$

Where:

$$S_{1pit} = 2 * \pi * r * h$$
$$r = \frac{\frac{a^2}{h} + h}{2}$$

a is the mean pit radius, h is the mean pit depth, Δt is the pulse duration, ρ_{Fe} is the density of iron , F is the faraday's constant and S_{1pit} is the surface of one pit (Fig. 15).

The experimental ($C_{corr-exp}$) and calculated (C_{corr}) densities of electric charge produced by the pit nucleation are presented in Table 3.

It is noteworthy that the experimental electric charge density measured during PPT ($C_{corr-exp}$) is two times lower than the theoretical one calculated with the model presented above (C_{corr}) (Table 3). Furthermore, values obtained for wrought material are roughly 10 times greater than those for SLM steel. That means that the measured current densities (Fig. 7 and 12) mainly come from the increase of the active surface due to the growth of pits.

Nevertheless, it is found that the expected density of electric charge C_{corr} is about twice as much as the experimental. This overestimation is because this modelling only includes the dissolution of the metal and does not take into account neither the double layer capacity of the material nor the effect of the passive film. Moreover, the different assumptions made on the pit geometry and the use of an average pit to represent all the pits may contribute to this higher value. This analysis shows that the measured current density reflects one part of the local damage mechanisms. A more elaborated modelling tacking into account all mechanisms could be considered. Nevertheless, at this stage, correlation between experimental measurements and pitting initiation and growth are relevant.

4.2. Role of the microstructure

The role of the microstructure on the susceptibility to pitting corrosion of wrought and SLM 316L is the subject of interest in this section. First of all, Fig. 16 shows 2D and 3D optical micrographs of pits on which depth profiles have been carried out. The pits created by PPT are essentially surface defects for wrought and SLM 316L. Indeed, the depth of the pits is at least 5 times smaller than their diameter (Fig. 16). In addition, the pit profiles on SLM 316L have a relatively spherical cap shape while the pits on wrought 316L present steeper edge. It is worth noting that the microstructure of the materials is seen at the bottom of the pits. For wrought 316L grain boundaries are observed while for SLM 316L the cellular-dendritic structures are visible (Fig. 11).

Figure 17 shows SEM observations after PPT on the wrought 316L where 30 potential jumps were applied only during 0.75 s to avoid initiating too large

pits. After this test, an etch was performed to reveal the microstructure of the material and to allow the location of the initiation sites. By analyzing the initiation sites of more than 90 pits using SEM and optical microscopy on the wrought 316L, it was noticed that 68% of the pitting occurs at grain boundaries (Fig. 17a) including 26% at triple boundaries (Fig. 17b).

In order to understand the reason of the greater sensitivity of the wrought 316L stainless steel grain boundaries, observations and chemical analyses were performed on a TEM equipped with an EDS detector.

The TEM observations and the EDS maps are displayed in Fig. 18. They show the presence of phases located at the grain boundaries which are richer in chromium and molybdenum and poorer in nickel and iron than the austenitic phase. This result is consistent with the Pryce and Andrew diagram [37] defined by the Cr and Ni equivalent contents which provides that the wrought 316L could contain small proportion of ferrite. Thus, as these phases could be ferrite, this EDS analysis is not indicative on the nature of these phases.

In any case, the presence of small phases located at grain boundaries may explain the greater susceptibility to pitting initiation at the interfaces between them and the austenite, probably related to different protective capacities of the passive film between phases [38, 39, 40].

Thus, pits certainly initiate at the interface between the enriched Cr and Mo phases and the austenite phase, then propagate by dissolution of the austenitic phase which is less resistant to corrosion. This progressive damage could explain the increase in current density responses for wrought AISI 316L stainless steel during the single PPT (Fig.7a, 7d and 7g).

The fishbone shape of the current evolution as a function of the number of pulses (Fig. 10a) could be explain by three complementary mechanisms :

1 - During the first pulses, the pits initiate more easily at the most weak sites of the passive film such the interfaces between the Cr and Mo rich phases located at the austenite grain boundaries.

2 - The pitting occuring during the first pulses leads to a progressive decrease of the number of weak sites.

3 - More pulses are needed to weaken the film in more resistant areas, resulting in the formation of smaller pits associated with a decrease in the current density response at each pulse (Fig. 14).

SLM 316L seems to contain neither various phases nor micrometric MnS inclusions which are known to be sites of pit initiation for wrought 316L steel [22, 41, 42, 43, 44, 45, 46, 47]. Indeed, Chao Qi et al. [22] found that rapid cooling of SLM 316L stainless steel prevents their formation. Besides, inclusions formed at the microscopic and nano scale [48, 27, 12] are not pit initiation sites because there is no chromium depletion zone created at their interface.

Even if the SLM process parameters and the powder have been optimized, some manufacturing defects were found such as porosities and unmelted metallic particles (Fig. 19). According to Man et al. [27] and Duan et al. [49], depending on environmental conditions, porosities and unmelted metallic particules are are pit initiation sites. However, observations performed after cyclic PPT show that porosities and unmelted metallic particules were not altered (Fig. 19). Under our operating conditions these defects

do not appear to be pit initiation sites. We rather observe a dissolution of the microstructure creating, according to Duan et al. [49], type 1 defects where the microstructure can be seen at the bottom of the pits (Fig. 11d, 11e and 11f). This type of corrosion may be due to a local weakness of the passive film, discussed in the following section.

The difference in corrosion susceptibility between SLM 316L and wrought 316L could be related to their residual stresses. Assessment of residual stresses by XRD revealed that the wrought and SLM 316L had compressive stress of -83 ± 32 and -64 ± 16 MPa, respectively. Residual stress values measured for 316L SLM are lower on average than those found in other studies that are more around -150 Mpa [22, 26, 50]. However, Vignal et al found quite similar values of -66 ± 24 and -24 ± 14 Mpa [51]. The observed difference in corrosion resistance between 316L SLM and wrought 316L may not be explained by this parameter. In addition, some authors such as Sanders et al. [26] and Cruz et al. [50] have shown that internal stress variation has a small impact on pitting corrosion of SLM 316L.

4.3. Role of the passive film

According to the chemical composition measurements (Table 1), Cr, Mo and Ni contents are higher for the SLM 316L than for the wrought 316L. It is well known that the corrosion resistance increases when Cr, Mo and Ni contents is improved, due to the formation of a more protective passive film leading to a decrease of the corrosion rate [38, 39, 40, 52, 53]. Thus, the difference of the chemical compositions of the studied alloys could, partially, explain the better corrosion resistance of SLM 316L.

Several studies dealing with the passive film have been carried out in or-

der to understand the origin of the better resistance to corrosion of SLM 316L [27, 54, 55, 56, 57]. Electrochemical impedance spectroscopy tests showed that 316L obtained by powder bed fusion has a higher resistivity than wrought 316L, reflecting better quality of the passive film [27, 57]. This better protection does not seem to come from the composition of the film. Indeed, using XPS measurements, Man et al. [27] found that the passive films of SLM and wrought 316L stainless steels have the same composition. However, using Auger Electron Spectroscopy (AES), they highlighted that the passive layer of SLM 316L is thicker than that of wrought 316L [27]. By coupling XPS and AES informations, they demonstrated that it is the thickness of the outer layer that is more important [27]. Kong et al. [25] found the same results on the passive film thickness by analyzing the capacitance obtained by electrochemical impedance spectroscopy. These various studies show that one of the causes of the increase in corrosion resistance of SLM 316L could be linked to an increase in the thickness of the oxide film, without any change in its composition.

The best passive film quality of the SLM 316L could be linked to its refined microstructure and to the presence of small inclusions which promote the nucleation of the passive films in environments favorable to passivation [27, 58, 59, 60]. These results are consistent with those presented in this study. Indeed, the current density response for the BD and ND SLM 316L begins with a peak followed by a decrease (Fig. 7b, 7c, 7e, 7f, 7h, 7i and Fig. 10b, 10c), unlike the wrought 316L (Fig. 7a, 7d, 7g and Fig. 10a). For the SLM 316L, the current density curves (Fig. 7 and Fig. 10) reflect an immediate local depassivation followed by a partial repassivation of the

pit surface, probably enhanced by the refined microstructure composed of cellular-dendritic structures. So, SLM and wrought 316L present different pitting mechanisms : initiated pits can not repassivate and can only grow for wrought 316L, whereas they have the ability to passivate themself for the SLM 316L.

As the number of pulses increases (Fig. 10), the current density peak at each pulse slightly raises for both BD and ND SLM 316L, showing that new pit initiation sites are continuously created at each pulse, without exhausting the sites. Moreover, pit diameter being the same regardless of the number of pulses (Fig. 14), previous pits are not initiation sites and no pit growth occurs by increasing the number of pulses.

However, a difference in sensitivity to pitting corrosion between the BD SLM and the ND SLM 316L is observed when the pulse duration or the number of pulses increases (Fig. 10b and 10c). Indeed, after the first current density peak, a secondary increase in current density is observed for ND SLM 316L resulting in a higher pit density than that of BD SLM 316L (Fig. 12 and Fig. 14b). The SLM material is therefore more susceptible to pitting corrosion in the normal direction. The slight increase of the first and second current density peaks as the number of pulses increases reflects a weakening of the SLM 316L's capacity to repassivate, while being more resistant to corrosion than wrought 316L (Fig. 10b and 10c). This phenomenon is most noticeable for the ND SLM 316L where a second depassivation is observed (Fig. 10b and 10c).

5. Conclusion

An original approach coupling PPT and statistical analysis of the pitting features was carried out to study the sensitivity to pitting corrosion of wrought and SLM 316L SS.

The measurement and analysis of current densities during PPT highlighted that SLM 316L is more resistant to pitting corrosion than wrought 316L in NaCl solution 4 mol.l^{-1} at 50 °C. Furthermore, the statistical analysis carried out on a large area (34mm^2) per sample showed that both stainless steels exhibit different pitting mechanisms. During a single PPT, pits mainly initiate at the interface between austenite and second nanoscale phases located at grain boundaries and grow during the pulse duration for wrought 316. For SLM 316L, pits may initiate and repassivate immediately due to the cellular-dendritic structures enhancing the passive film formation.

The best resistance to pitting corrosion of the SLM 316L is also observed after successive depassivation and repassivation cycles due to its good passive film formation capacity.

Moreover, these tests highlighted that the passive film properties depend on the manufacturing direction. As a result, ND SLM 316L is slightly more susceptible to pitting corrosion than BD SLM 316L.

6. Acknowledgment

This work was a part of the Project OCEAN (Optimization and Conception for a mEthodology AdvaNced) in ALM (Additive Layer Manufacturing). It was financially supported by the French Region Nouvelle-Aquitaine and the CEA (Commissariat à l'Energie Atomique et aux énergies alternatives).

References

[1] C. Kamath, B. El-dasher, G. F. Gallegos, W. E. King, A. Sisto, Density of additively-manufactured, 316L SS parts using laser powder-bed fusion at powers up to 400 W, The International Journal of Advanced Manufacturing Technology 74 (1-4) (2014) 65–78. doi:10.1007/s00170-014-5954-9.

[2] G. Scotti, V. Matilainen, P. Kanninen, H. Piili, A. Salminen, T. Kallio, S. Franssila, Laser additive manufacturing of stainless steel micro fuel cells, Journal of Power Sources 272 (2014) 356–361. doi:10.1016/j.jpowsour.2014.08.096.

[3] K. Refai, C. Brugger, M. Montemurro, N. Saintier, An experimental and numerical study of the high cycle multiaxial fatigue strength of titanium lattice structures produced by selective laser melting (slm), International Journal of Fatigue (2020) 105623.

[4] D. Herzog, V. Seyda, E. Wycisk, C. Emmelmann, Additive manufacturing of metals, Acta Materialia 117 (2016) 371–392. doi:10.1016/j.actamat.2016.07.019.

[5] K. Zhang, W. Liu, X. Shang, Research on the processing experiments of laser metal deposition shaping, Optics & Laser Technology 39 (3) (2007) 549–557. doi:10.1016/j.optlastec.2005.10.009.

[6] B. Zhang, L. Dembinski, C. Coddet, The study of the laser parameters and environment variables effect on mechanical properties of high compact parts elaborated by selective laser melting 316L

powder, Materials Science and Engineering: A 584 (2013) 21–31. doi:10.1016/j.msea.2013.06.055.

[7] W. Gao, Y. Zhang, D. Ramanujan, K. Ramani, Y. Chen, C. B. Williams, C. C. Wang, Y. C. Shin, S. Zhang, P. D. Zavattieri, The status, challenges, and future of additive manufacturing in engineering, Computer-Aided Design 69 (2015) 65–89. doi:10.1016/j.cad.2015.04.001.

[8] W. J. Sames, F. A. List, S. Pannala, R. R. Dehoff, S. S. Babu, The metallurgy and processing science of metal additive manufacturing, International Materials Reviews 61 (5) (2016) 315–360. doi:10.1080/09506608.2015.1116649.

[9] C.-O. Olsson, D. Landolt, Passive films on stainless steels—chemistry, structure and growth, Electrochimica Acta 48 (9) (2003) 1093–1104. doi:10.1016/S0013-4686(02)00841-1.

[10] K. Sugimoto, Simulation analysis of electrochemical nature of real passive films with artificial passivation films, Corrosion Science 49 (1) (2007) 63–71. doi:10.1016/j.corsci.2006.05.007.

[11] Y. Yang, Y. Zhu, M. Khonsari, H. Yang, Wear anisotropy of selective laser melted 316L stainless steel, Wear 428-429 (2019) 376–386. doi:10.1016/j.wear.2019.04.001.

[12] K. Saeidi, X. Gao, Y. Zhong, Z. Shen, Hardened austenite steel with columnar sub-grain structure formed by laser melting, Materials Science and Engineering: A 625 (2015) 221–229. doi:10.1016/j.msea.2014.12.018.

[13] M. Shamsujjoha, S. R. Agnew, J. M. Fitz-Gerald, W. R. Moore, T. A. Newman, High Strength and Ductility of Additively Manufactured 316L Stainless Steel Explained, Metallurgical and Materials Transactions A 49 (7) (2018) 3011–3027. doi:10.1007/s11661-018-4607-2.

[14] Y. Sun, A. Moroz, K. Alrbaey, Sliding Wear Characteristics and Corrosion Behaviour of Selective Laser Melted 316L Stainless Steel, Journal of Materials Engineering and Performance 23 (2) (2014) 518–526. doi:10.1007/s11665-013-0784-8.

[15] Y. Zhong, L.-E. Rännar, L. Liu, A. Koptyug, S. Wikman, J. Olsen, D. Cui, Z. Shen, Additive manufacturing of 316L stainless steel by electron beam melting for nuclear fusion applications, Journal of Nuclear Materials 486 (2017) 234–245. doi:10.1016/j.jnucmat.2016.12.042.

[16] M. Montero Sistiaga, S. Nardone, C. Hautfenne, J. Van Humbeeck, Effect of heat treatment of 316l stainless steel produced by selective laser melting (slm), in: Proceedings of the 27th Annual International Solid Freeform Fabrication Symposium-An Additive Manufacturing Conference, 2016, pp. 558–565.

[17] J. R. Trelewicz, G. P. Halada, O. K. Donaldson, G. Manogharan, Microstructure and corrosion resistance of laser additively manufactured 316l stainless steel, Jom 68 (3) (2016) 850–859.

[18] E. Yasa, J.-P. Kruth, Microstructural investigation of Selective Laser Melting 316L stainless steel parts exposed to laser re-melting, Procedia Engineering 19 (2011) 389–395. doi:10.1016/j.proeng.2011.11.130.

[19] D. Wang, C. Song, Y. Yang, Y. Bai, Investigation of crystal growth mechanism during selective laser melting and mechanical property characterization of 316L stainless steel parts, Materials & Design 100 (2016) 291–299. doi:10.1016/j.matdes.2016.03.111.

[20] J. Schultze, M. Lohrengel, Stability, reactivity and breakdown of passive films. Problems of recent and future research, Electrochimica Acta 45 (15-16) (2000) 2499–2513. doi:10.1016/S0013-4686(00)00347-9.

[21] G. Sander, S. Thomas, V. Cruz, M. Jurg, N. Birbilis, X. Gao, M. Brameld, C. R. Hutchinson, On The Corrosion and Metastable Pitting Characteristics of 316L Stainless Steel Produced by Selective Laser Melting, Journal of The Electrochemical Society 164 (6) (2017) C250–C257. doi:10.1149/2.0551706jes.

[22] Q. Chao, V. Cruz, S. Thomas, N. Birbilis, P. Collins, A. Taylor, P. D. Hodgson, D. Fabijanic, On the enhanced corrosion resistance of a selective laser melted austenitic stainless steel, Scripta Materialia 141 (2017) 94–98. doi:10.1016/j.scriptamat.2017.07.037.

[23] M. Zietala, T. Durejko, M. Polanski, I. Kunce, T. Plocinski, W. Zielinski, M. Lazinska, W. Stepniowski, T. Czujko, K. J. Kurzydlowski, Z. Bojar, The microstructure, mechanical properties and corrosion resistance of 316L stainless steel fabricated using laser engineered net shaping, Materials Science and Engineering: A 677 (2016) 1–10. doi:10.1016/j.msea.2016.09.028.

[24] P. Ganesh, R. Giri, R. Kaul, P. Ram Sankar, P. Tiwari, A. At-

ulkar, R. Porwal, R. Dayal, L. Kukreja, Studies on pitting corrosion and sensitization in laser rapid manufactured specimens of type 316L stainless steel, Materials & Design 39 (2012) 509–521. doi:10.1016/j.matdes.2012.03.011.

[25] D. Kong, X. Ni, C. Dong, X. Lei, L. Zhang, C. Man, J. Yao, X. Cheng, X. Li, Bio-functional and anti-corrosive 3D printing 316L stainless steel fabricated by selective laser melting, Materials & Design 152 (2018) 88–101. doi:10.1016/j.matdes.2018.04.058.

[26] G. Sander, A. Babu, X. Gao, D. Jiang, N. Birbilis, On the effect of build orientation and residual stress on the corrosion of 316l stainless steel prepared by selective laser melting, Corrosion Science 179 (2021) 109149.

[27] C. Man, C. Dong, T. Liu, D. Kong, D. Wang, X. Li, The enhancement of microstructure on the passive and pitting behaviors of selective laser melting 316L SS in simulated body fluid, Applied Surface Science 467-468 (2019) 193–205. doi:10.1016/j.apsusc.2018.10.150.

[28] S.-H. Sun, T. Ishimoto, K. Hagihara, Y. Tsutsumi, T. Hanawa, T. Nakano, Excellent mechanical and corrosion properties of austenitic stainless steel with a unique crystallographic lamellar microstructure via selective laser melting, Scripta Materialia 159 (2019) 89–93. doi:10.1016/j.scriptamat.2018.09.017.

[29] V. Vignal, S. Bissey-Breton, J.-B. Coudert, Mechanical properties and corrosion behaviour of low carbon martensitic stainless steel after ma-

chining, International Journal of Machining and Machinability of Materials 7 15 (1-2) (2014) 36–53.

[30] J. Kang, G. Frankel, Potentiostatic pulse testing for assessment of early coating failure, Zeitschrift für Physikalische Chemie 219 (11) (2005) 1519–1537.

[31] Y. Sun, L. Sun, N. Dai, Y. Liu, J. Wu, J. Li, Y. Jiang, Application of potentiostatic pulse technique and statistical analysis in evaluating pitting resistance of aged 317l stainless steel, Materials and Corrosion 71 (6) (2020) 900–908.

[32] B. Chen, Y. Sun, D. Cai, Q. Yao, L. Yin, Y. Wan, Y. Jiang, J. Li, Use of the potentiostatic pulse technique to study and influence pitting behavior of 317l stainless steel, Journal of The Electrochemical Society 167 (4) (2020) 041509.

[33] J. Gao, Y. Jiang, B. Deng, Z. Ge, J. Li, Determination of pitting initiation of duplex stainless steel using potentiostatic pulse technique, Electrochimica Acta 55 (17) (2010) 4837–4844.

[34] V. Vignal, S. Ringeval, S. Thiébaut, K. Tabalaiev, C. Dessolin, O. Heintz, F. Herbst, R. Chassagnon, Influence of the microstructure on the corrosion behaviour of low-carbon martensitic stainless steel after tempering treatment, Corrosion Science 85 (2014) 42–51. doi:10.1016/j.corsci.2014.03.036.

[35] V. Vignal, V. Richoux, E. Suzon, S. Thiébaut, K. Tabaleiv, The use of potentiostatic pulse testing to study the corrosion behavior of welded

stainless steels in sodium chloride solution, Materials & Design 88 (2015) 186–195. doi:10.1016/j.matdes.2015.09.001.

[36] R. D. Granata, K. J. Kovaleski, Evaluation of high-performance protective coatings by electrochemical impedance and chronoamperometry, in: Electrochemical Impedance: Analysis and Interpretation, ASTM International, 1993.

[37] L. Pryce, Practical estimation of composition balance and ferrite content in stainless steels, J Iron Steel Inst 195 (1960) 415–417.

[38] A. Sedriks, Plenary lecture—1986: Effects of alloy composition and microstructure on the passivity of stainless steels, Corrosion 42 (7) (1986) 376–389.

[39] Y. Kobayashi, S. Virtanen, H. Bohni, Microelectrochemical studies on the influence of cr and mo on nucleation events of pitting corrosion, Journal of the Electrochemical Society 147 (1) (2000) 155.

[40] C.-O. Olsson, D. Landolt, Passive films on stainless steels—chemistry, structure and growth, Electrochimica acta 48 (9) (2003) 1093–1104.

[41] C. Man, C. Dong, K. Xiao, Q. Yu, X. Li, The combined effect of chemical and structural factors on pitting corrosion induced by mns-(cr, mn, al) o duplex inclusions, Corrosion 74 (3) (2018) 312–325.

[42] B. Vuillemin, X. Philippe, R. Oltra, V. Vignal, L. Coudreuse, L. Dufour, E. Finot, Svet, afm and aes study of pitting corrosion initiated on mns inclusions by microinjection, Corrosion science 45 (6) (2003) 1143–1159.

[43] J. Castle, R. Ke, Studies by auger spectroscopy of pit initiation at the site of inclusions in stainless steel, Corrosion science 30 (4-5) (1990) 409–428.

[44] M. Baker, J. Castle, The initiation of pitting corrosion of stainless steels at oxide inclusions, Corrosion science 33 (8) (1992) 1295–1312.

[45] M. Baker, J. Castle, The initiation of pitting corrosion at mns inclusions, Corrosion Science 34 (4) (1993) 667–682.

[46] H. Krawiec, V. Vignal, O. Heintz, R. Oltra, J.-M. Olive, Influence of the chemical dissolution of mns inclusions on the electrochemical behavior of stainless steels, Journal of the Electrochemical Society 152 (7) (2005) B213.

[47] T. S. L. Wijesinghe, D. J. Blackwood, Real time pit initiation studies on stainless steels: the effect of sulphide inclusions, Corrosion Science 49 (4) (2007) 1755–1764.

[48] X. Lou, P. L. Andresen, R. B. Rebak, Oxide inclusions in laser additive manufactured stainless steel and their effects on impact toughness and stress corrosion cracking behavior, Journal of Nuclear Materials 499 (2018) 182–190. doi:10.1016/j.jnucmat.2017.11.036.

[49] Z. Duan, C. Man, C. Dong, Z. Cui, D. Kong, X. Wang, et al., Pitting behavior of slm 316l stainless steel exposed to chloride environments with different aggressiveness: Pitting mechanism induced by gas pores, Corrosion Science (2020) 108520.

[50] V. Cruz, Q. Chao, N. Birbilis, D. Fabijanic, P. Hodgson, S. Thomas, Electrochemical studies on the effect of residual stress on the corrosion of 316l manufactured by selective laser melting, Corrosion Science 164 (2020) 108314.

[51] V. Vignal, C. Voltz, S. Thiébaut, M. Demésy, O. Heintz, S. Guerraz, Pitting corrosion of type 316l stainless steel elaborated by the selective laser melting method: Influence of microstructure, Journal of Materials Engineering and Performance (2021) 1–9.

[52] J. Hayes, J. Gray, A. Szmodis, C. Orme, Influence of chromium and molybdenum on the corrosion of nickel-based alloys, Corrosion 62 (6) (2006) 491–500.

[53] A. Pardo, M. Merino, A. Coy, F. Viejo, R. Arrabal, E. Matykina, Pitting corrosion behaviour of austenitic stainless steels–combining effects of mn and mo additions, Corrosion Science 50 (6) (2008) 1796–1806.

[54] D. Kong, X. Ni, C. Dong, L. Zhang, C. Man, J. Yao, K. Xiao, X. Li, Heat treatment effect on the microstructure and corrosion behavior of 316L stainless steel fabricated by selective laser melting for proton exchange membrane fuel cells, Electrochimica Acta 276 (2018) 293–303. doi:10.1016/j.electacta.2018.04.188.

[55] F. Andreatta, A. Lanzutti, E. Vaglio, G. Totis, M. Sortino, L. Fedrizzi, Corrosion behaviour of 316l stainless steel manufactured by selective laser melting, Materials and Corrosion 70 (9) (2019) 1633–1645.

[56] M. Lodhi, K. Deen, W. Haider, Corrosion behavior of additively manufactured 316L stainless steel in acidic media, Materialia 2 (2018) 111–121. doi:10.1016/j.mtla.2018.06.015.

[57] M. Lodhi, K. Deen, M. Greenlee-Wacker, W. Haider, Additively manufactured 316L stainless steel with improved corrosion resistance and biological response for biomedical applications, Additive Manufacturing 27 (2019) 8–19. doi:10.1016/j.addma.2019.02.005.

[58] S. Gollapudi, Grain size distribution effects on the corrosion behaviour of materials, Corrosion Science 62 (2012) 90–94.

[59] T. Li, L. Liu, B. Zhang, Y. Li, F. Wang, An investigation on the continuous and uniform thin membrane passive film formed on sputtered nanocrystalline stainless steel, Corrosion Science 104 (2016) 71–83.

[60] M. Gaberšček, S. Pejovnik, Impedance spectroscopy as a technique for studying the spontaneous passivation of metals in electrolytes, Electrochimica acta 41 (7-8) (1996) 1137–1142.

Elements	C	N	S	Cr	Mn	Mo	Ni	P	Si	Fe
Wrought 316L	0.016	0.031	0.0008	16.7	1.51	1.96	9.8	0.03	0.56	Bal.
SLM 316L	0.010	0.048	0.005	17.7	0.38	2.38	12.7	0.011	0.41	Bal.

Table 1: Chemical composition of 316L wrought and 316L SLM (wt%)

Material	316L Wrought	BD SLM 316L	ND SLM 316L
$\mathbf{E}_{corr}$	- 106 ± 8	- 110 ± 20	-108 ± 20
$\mathbf{E}_{pit}$	104 ± 12	580 ± 30	590 ± 40
$\mathbf{\Delta E}$	210 ± 20	690 ± 50	700 ± 60
$\mathbf{E}_{rep}$	-15 ± 10	-17 ± 14	-12 ± 13

Table 2: Polarization curves parameters

Material	316L Wrought	BD SLM 316L	ND SLM 316L
$\mathbf{C}_{corr-exp}$ **(C.mm^2)**	2.6 ± 0.3	0.22 ± 0.10	0.34 ± 0.12
$\mathbf{C}_{corr}$ **(C.mm^2)**	5.1	0.48	0.72

Table 3: Density of electric charge measured during a 2s pulse tests ($C_{corr-exp}$), and expected electric charge density (C_{corr}) induced by a single potensiostatic pulse of 2s.

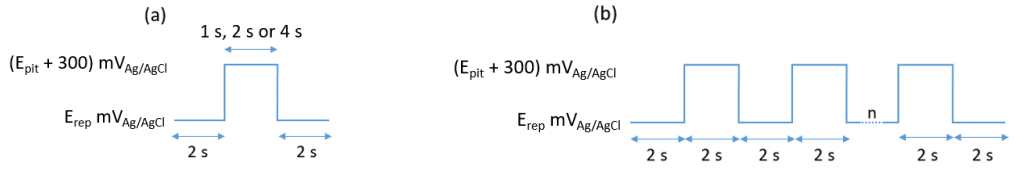

Figure 1: (a) Single potentiostatic pulse test (b), cyclic potentiostatic pulse test

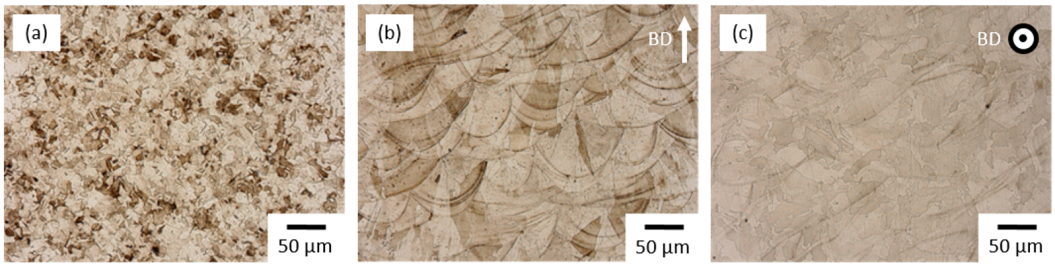

Figure 2: Optical micrographs of 316L SS, (a) wrought 316L SS, (b) As-built BD SLM 316L SS, (c) As-built ND SLM 316L SS

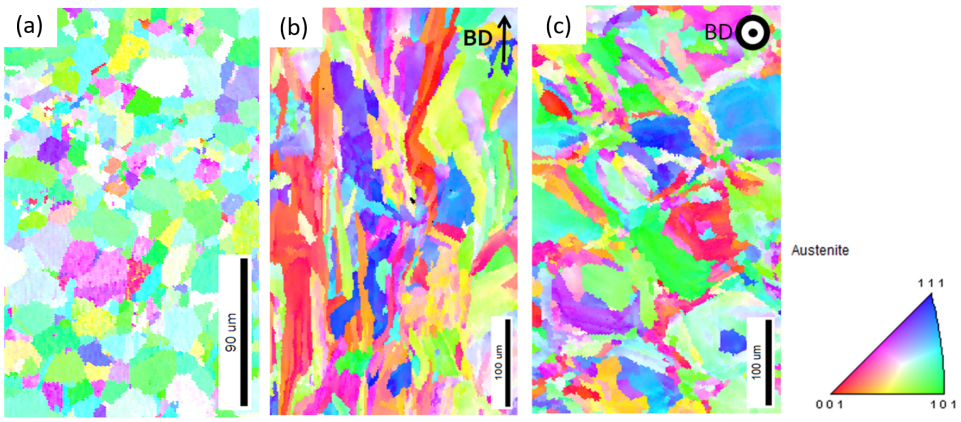

Figure 3: Orientation imaging microscopy maps of wrought and SLM 316L SS (a) As-built BD SLM 316L SS, (b)As-built ND SLM 316L SS and (c) Wrought 316L

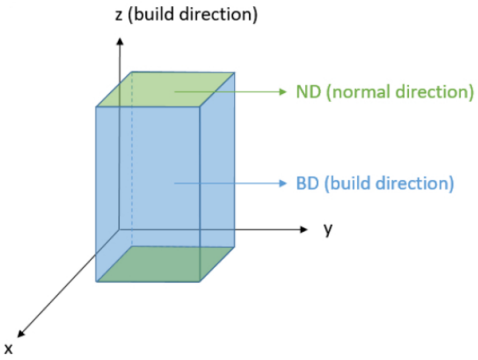

Figure 4: Surface naming of samples obtained by SLM

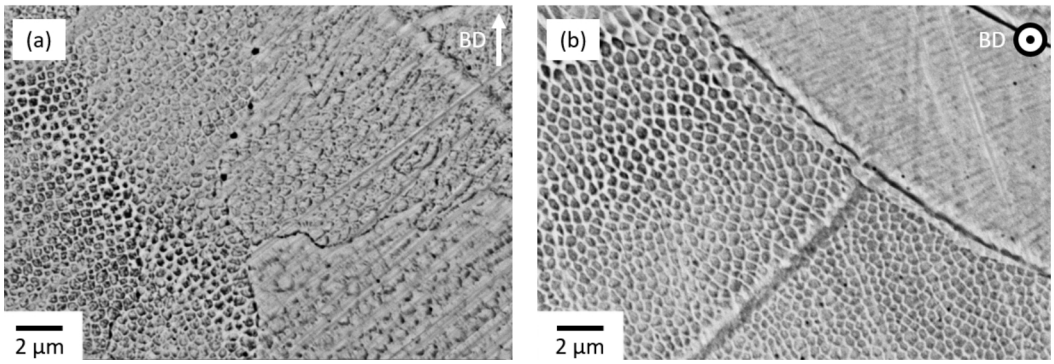

Figure 5: SEM micrographs of SLM 316L stainless steel (a) As-built BD SLM 316L SS, (b) As-built ND SLM 316L SS

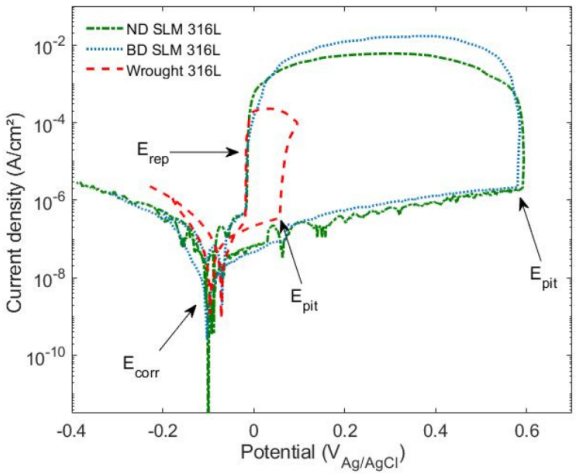

Figure 6: Cyclic polarisation curves of 316L stainless steel in 4 mol.l^{-1} of NaCl at 50 °C. Scan rate 1 mV/s

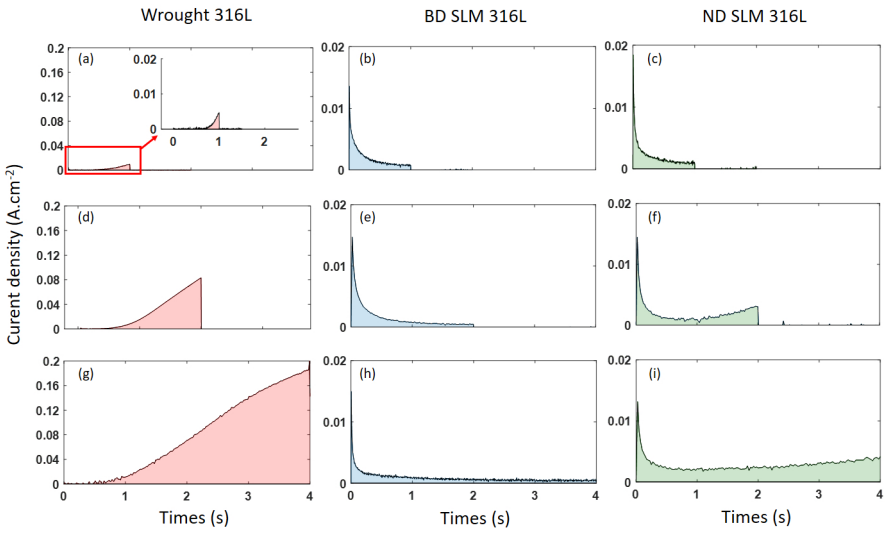

Figure 7: Current density response during a potential disturbance of + 300 mV/E_{pit}, (a) wrought 316L with 1 s disturbance, (b) BD SLM 316L with 1 s disturbance, (c) ND SLM 316L with 1 s disturbance, (d) wrought 316L with 2 s disturbance, (e) BD SLM 316L with 2 s disturbance, (f) ND SLM 316L with 2 s disturbance, (g) wrought 316L with 4 s disturbance, (h) BD SLM 316L with 4 s disturbance, (i) ND SLM 316L with 4 s disturbance

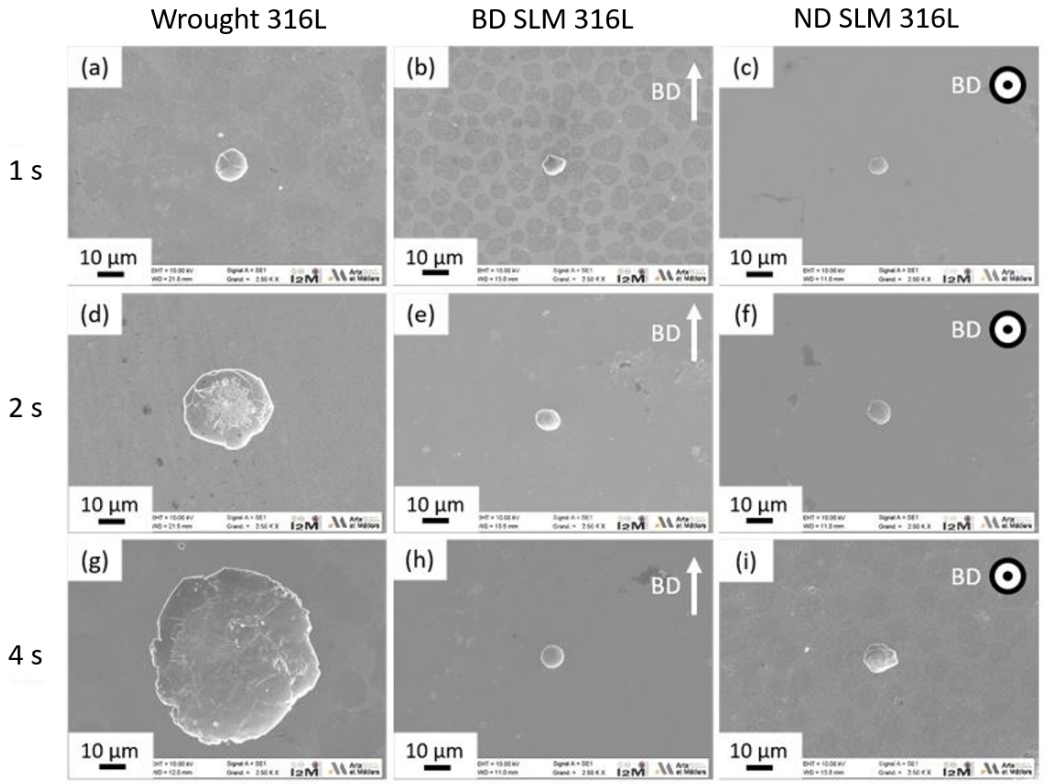

Figure 8: SEM micrographs after potential disturbance of + 300 mV/E_{pit}, (a) wrought 316L 1 s disturbance, (b) BD SLM 316L 1 s disturbance, (c) ND SLM 316L 1 s disturbance,(d) wrought 316L 2 s disturbance, (e) BD SLM 316L 2 s disturbance, (f) ND SLM 316L 2 s disturbance, (g) wrought 316L 4 s disturbance, (h) BD SLM 316L 4 s disturbance, (i) ND SLM 316L 4 s disturbance

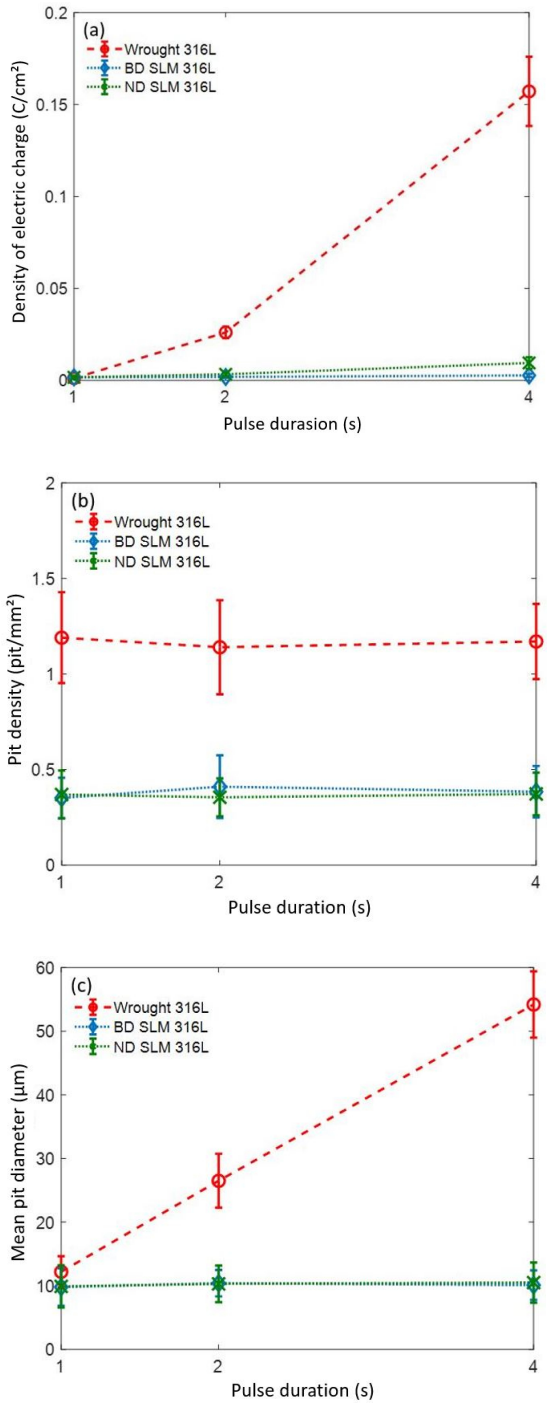

Figure 9: Density of electric charge and statistical analysis of pit size and density, (a) Density of electric charge obtained by calculating the area under the current density response curve (Fig. 7) as a function of pulse duration, (b) pit density obtained by analysis of sample surface as a function of pulse duration and (c) average pit diameter obtained by analysis of sample surface as a function of pulse duration

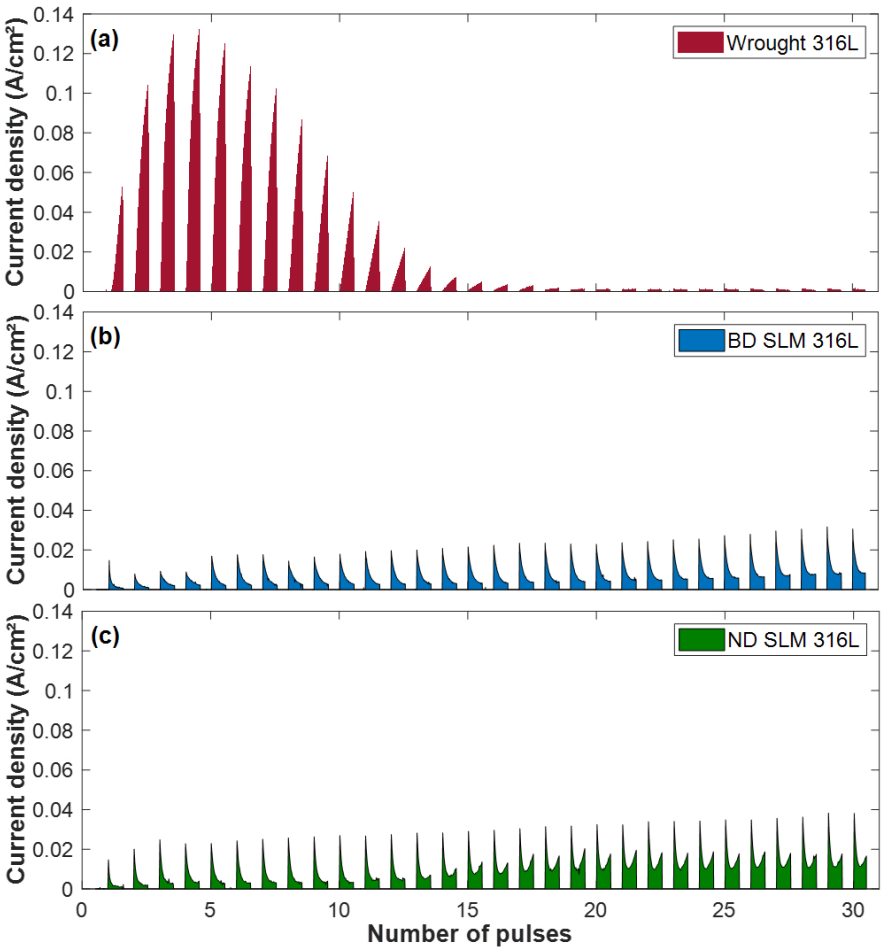

Figure 10: Current density of 30 potential disturbance cycles (pulses) at E_{pit} + 300 mV, (a) wrought 316L, (b) BD SLM 316L, (c) ND SLM 316L

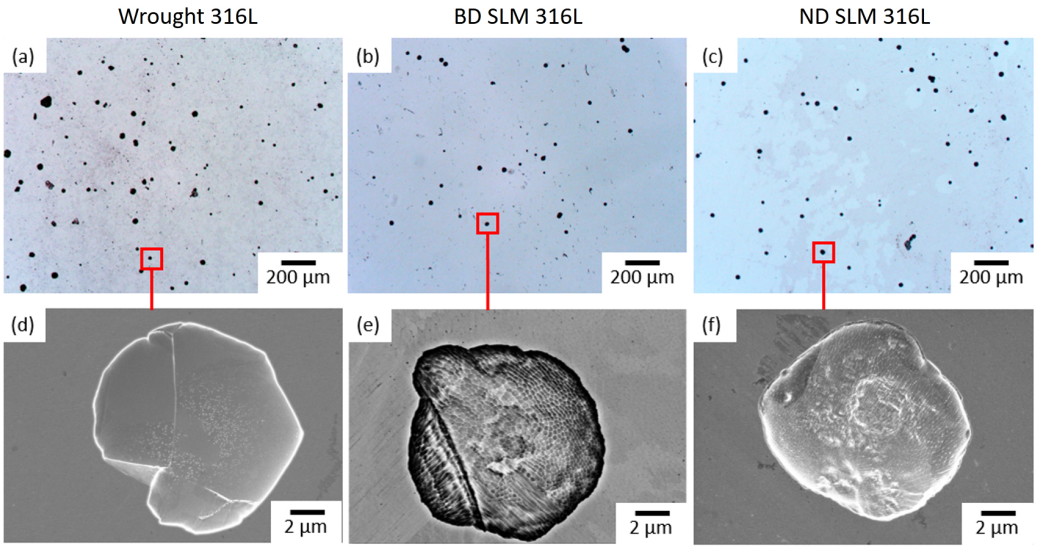

Figure 11: Optical micrography after 30 pulses at E_{pit} + 300 mV , (a) wrought 316L, (b) BD SLM 316L, (c) ND SLM 316L and SEM micrographs after 30 pulses at E_{pit} + 300 mV, (d) wrought 316L, (e) BD SLM 316L, (f) ND SLM 316L

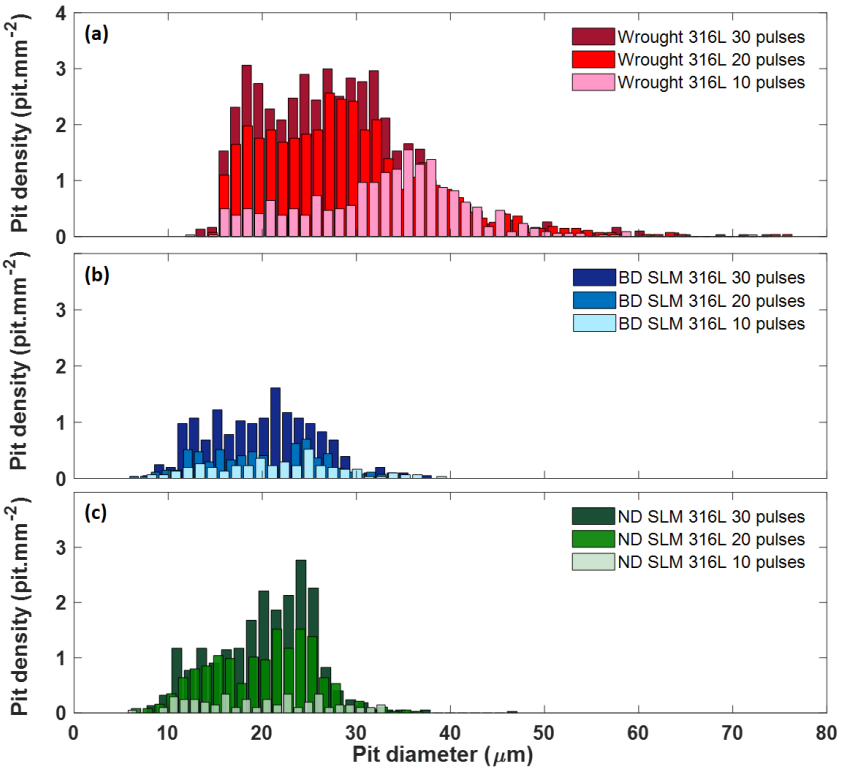

Figure 12: histograms of pit density versus pit diameter for 10, 20 and 30 pulses. (a) wrought 316L, (b) BD SLM 316L and (c) ND SLM 316L

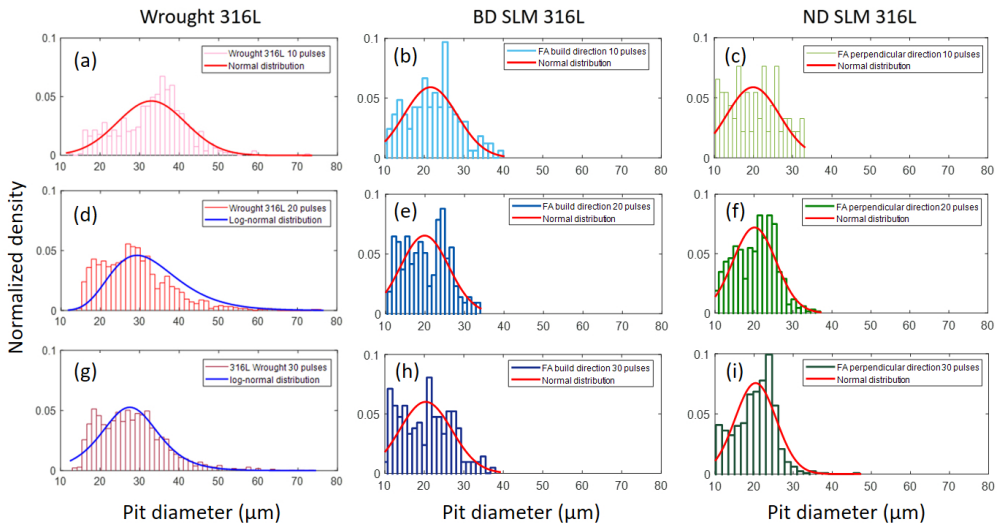

Figure 13: histograms of pit density versus pit diameter for wrought 316L, BD SLM 316L and ND SLM 316L. Red curves represent the corresponding theoretical normal curves and blue curves represent the corresponding theoretical log-normal curves, (a) wrought 316L 10 pulses, (b) BD SLM 316L 10 pulses, (c) ND SLM 316L 10 pulses,(d) wrought 316L 20 pulses, (e) BD SLM 316L 20 pulses, (f) ND SLM 316L 20 pulses, (g) wrought 316L 30 pulses, (h) BD SLM 316L 30 pulses, (i) ND SLM 316L 30 pulses

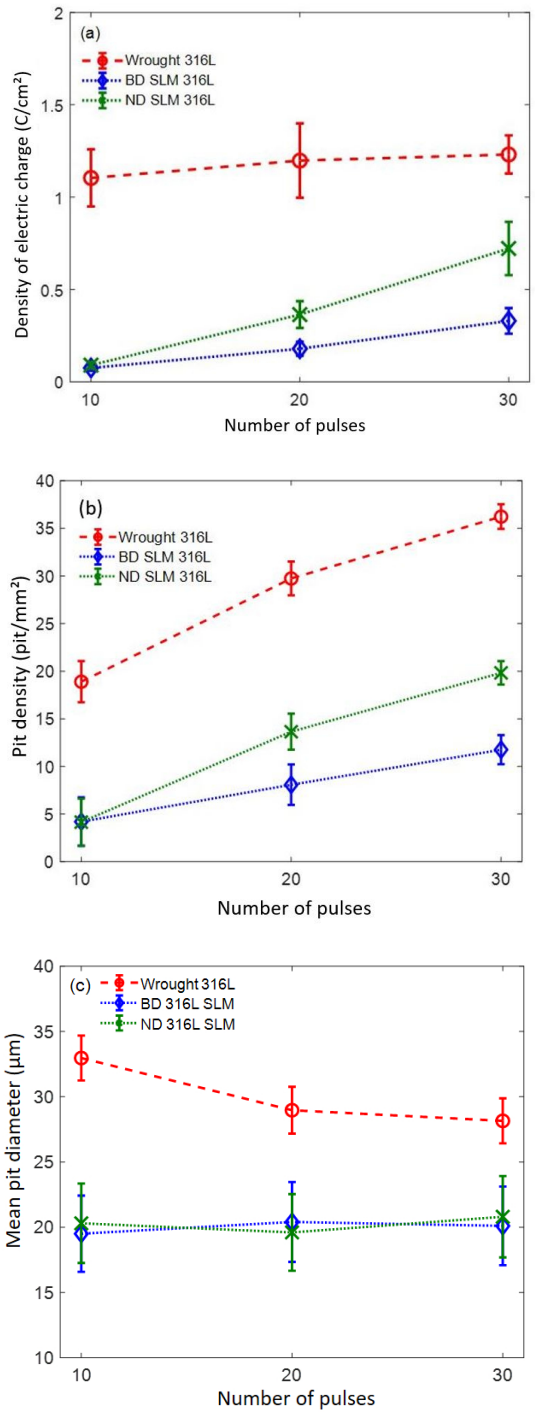

Figure 14: Density of electric charge and statistical analysis of pit size and density, (a) density of electric charge obtained by calculating the area under the current density response curve (Fig. 10) versus pulses number, (b) pit density obtained by analysis of sample surface versus pulses number and (c) average pit diameter obtained by analysis of sample surface versus pulses number

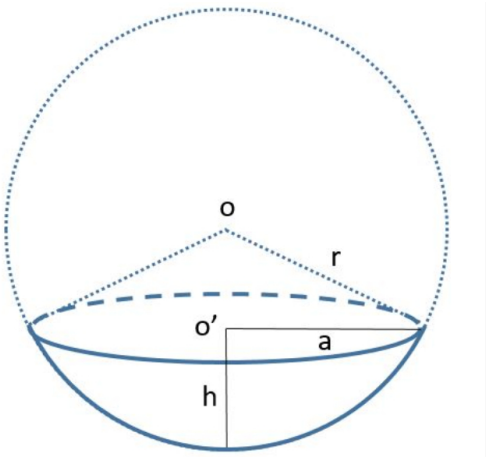

Figure 15: Pit volume based on the assumption of a spherical cap shape.

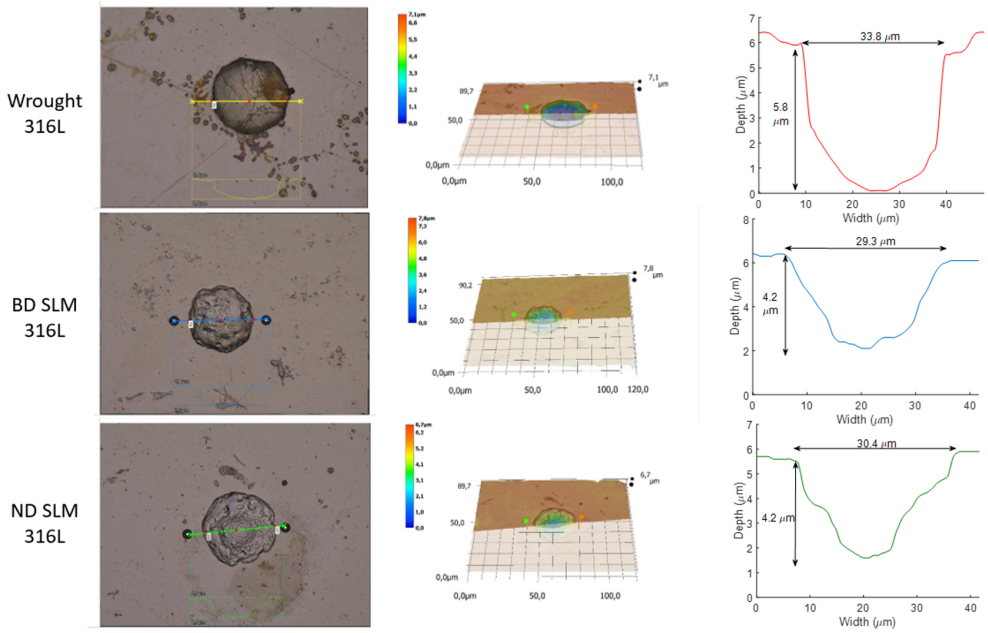

Figure 16: Pitting 3D morphologies and depth of the wrought 316L, BD SLM 316L and ND SLM 316L after 10 cycles potentiostatic pulse tests in 4M NaCl at 50 °C

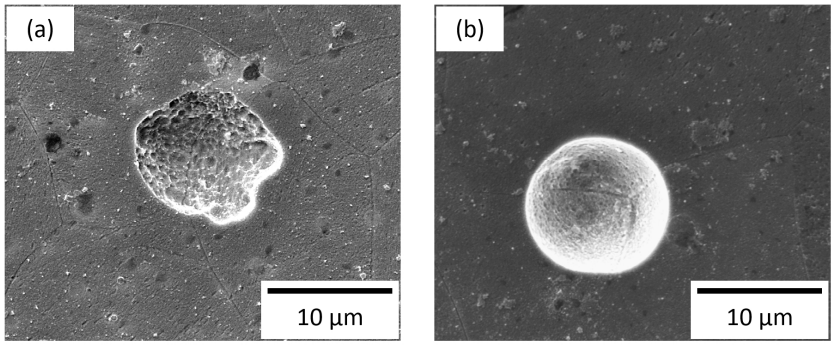

Figure 17: SEM image of an exemple pit after chemical etching of the microstructure on wrought 316L, (a) SEM image at grain boundaries, (b) SEM image at triple grain boundaries

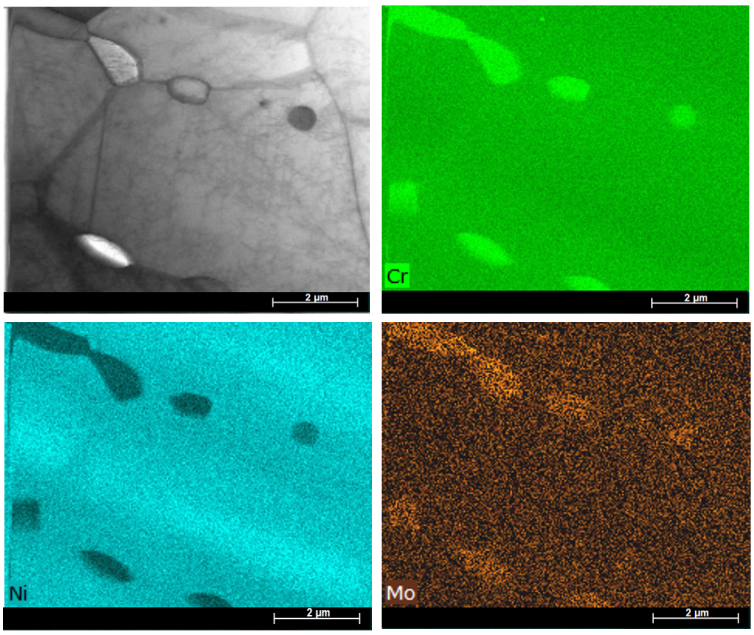

Figure 18: TEM observations and the EDS maps for wrought 316L stainless steel

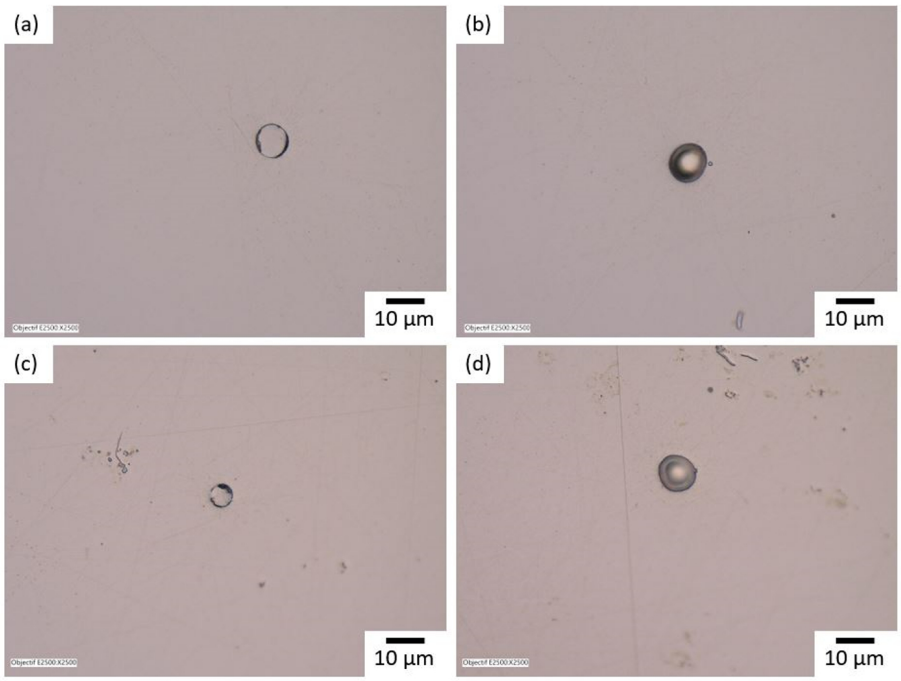

Figure 19: Defect on BD SLM 316L: (a) unmelted metallic particule and (b) porosity after polishing of the surface, (c) unmelted metallic particule and (d) porosity after 10 cycle potentiostatic pulse tests in 4 mol.l^{-1} NaCl at 50 °C

Graphical Abstract

Statistical analysis of the pitting corrosion induced by potentiostatic pulse tests of wrought and SLM 316L stainless steels

Arthur Racot, Isabelle Aubert, Marie Touzet, Stephanie Thiebaut, Michel Demesy

Highlights

Statistical analysis of the pitting corrosion induced by potentiostatic pulse tests of wrought and SLM 316L stainless steels

Arthur Racot, Isabelle Aubert, Marie Touzet, Stephanie Thiebaut, Michel Demesy

- Pitting corrosion sensitivity of wrought and SLM 316L stainless steels during depassivation-repassivation cycles.
- Current density responses of wrought and SLM 316L SS induced by single and cyclic potentiostatic pulse tests.
- Statistical analysis of the pitting corrosion feature (density and diameter of pits) induced by single and cyclic pulse tests.
- Difference of pitting sensitivity between the two SLM manufacturing directions (build direction and normal direction)